Supplementary information (SI)

Trifluoromethyl group incorporated spacer in 2D perovskite-based photodetectors with good responsivity and a big Pb–I–Pb bond angle: the first example of an aliphatic linearly-chained spacer forming non-classical hydrophobic hydrogen bonding

Gurumallappa Gurumallappa,[a,b] Norman Lu,*[a,b,c] Yi-De Chen,[a] Yu-Ching Lin,[a] Yueh-Fang Hsiao,[a] Pin-Yu Liu,[a] Meng-Lin Tsai[d]

[a.] *Institute of Organic and Polymeric Materials, National Taipei University of Technology, Taipei 106, Taiwan (ROC).*
[b.] *Graduate Institute of Energy and Optoelectronic Materials National Taipei University of Technology, Taipei 106, Taiwan (ROC).*
[c.] *Department of Molecular Science and Engineering, National Taipei University of Technology, Taipei 106, Taiwan (ROC).*
[d.] *Department of Materials Science and Engineering, National Taiwan University of Science and Technology, Taipei 106335, Taiwan (ROC).*

TABLE OF CONTENTS

1. Synthesis of materials

1.1. Chemistry SI-3
1.2. Synthesis of N-BOC-PA-OH (**1**) SI-3
1.3. Synthesis of N-BOC-PA-Br (**2**) SI-4
1.4. Synthesis of N-BOC-3F-PA-ligand (**3**) SI-5
1.5. Synthesis of fluorinated 3F-PA·HI salt (**4**) SI-6
1.6. Preparation of $(3F\text{-}PAH)_2PbI_4$ HP precursor solution SI-6
1.7. Characterization of $(3F\text{-}PAH)_2PbI_4$ perovskite SI-6
1.8. Device fabrication and measurements SI-7

2. Computational study

Computational method SI-7

3. Characterization

Figure S1. The HOMO and LUMO diagram of fluorinated $3F\text{-}PAH^+$ organic cation SI-8
Figure S2. The photo-images of the synthesized $(3F\text{-}PAH)_2PbI_4$ HP single-crystals SI-8
Figure S3. The Pb−I bond lengths and the I−Pb−I bond of the $[PbI_6]^{4-}$ octahedra SI-9
Figure S4. The packing mode with the space-filling view of $(3F\text{-}PAH)_2PbI_4$ HP SI-10
Figure S5. The simulated PXRD pattern of fluorinated $(3F\text{-}PAH)_2PbI_4$ HP SI-9
Figure S6. The the thickness of the $(3F\text{-}PAH)_2PbI_4$ HP film SI-10
Figure S7. EDS spectrum and EDS-mapping of $(3F\text{-}PAH)_2PbI_4$ HP film SI-11
Figure S8. The surface morphology of the$(BA)_2PbI_4$ HP film SI-11
Figure S9. Cyclic voltammetry (CV) profile of fluorinated $(3F\text{-}PAH)_2PbI_4$ HP SI-12
Figure S10. Schematic energy band diagram of the $(3F\text{-}PAH)_2PbI_4$ HP SI-12
Figure S11. The PL spectrum of the fluorinated $(3F\text{-}PAH)_2PbI_4$ HP film SI-13
Figure S12. Schematic illustration of the $(3F\text{-}PAH)_2PbI_4$ HP device SI-13
Figure S13. *I-V* characteristics of the $(3F\text{-}PAH)_2PbI_4$ HP device under 450 nm SI-14
Figure S14. *I-V* characteristics of $(3F\text{-}PAH)_2PbI_4$ HP device under dark conditions SI-14
Figure S15. Photodetection testing of the $(3F\text{-}PAH)_2PbI_4$ HP device under 520 nm SI-15

4. Structural table section

Table S1. X-ray crystallographic data of $(3F\text{-}PAH)_2PbI_4$ HP SI-16
Table S2. Selected bond lengths in $(3F\text{-}PAH)_2PbI_4$ HP SI-17
Table S3. Selected bond angles in $(3F\text{-}PAH)_2PbI_4$ HP SI-18
Table S4. N−H···I and C−H···Y type of hydrogen bonds in $(3F\text{-}PAH)_2PbI_4$ HP SI-19
Table S5. Comparison of structural and optical properties of $(3F\text{-}PAH)_2PbI_4$ HP SI-20
Table S6. Calculated crystallite size of $(3F\text{ -}PAH)_2PbI_4$ HP SI-20
Table S7. Comparison of hydrophobic and hydrophilic HB interactions SI-21
Table S8. Comparison of TRPL parameters of $(3F\text{-}PAH)_2PbI_4$ HP SI-22

5. The NMR Spectra of prepared compounds

Figure S16. ^1H NMR spectrum of N-BOC-PA-OH (**1**) SI-23

Figure S17. ^{1}H NMR spectrum of N-BOC-PA-Br (**2**) SI-23
Figure S18. ^{1}H NMR spectrum of N-BOC-3F-PA-ligand (**3**) SI-24
Figure S19. ^{1}H NMR spectrum of 3F-PA·HI salt (**4**) SI-24
Figure S20. ^{13}C NMR spectrum of 3F-PA·HI salt (**4**) SI-25
Figure S21. ^{19}F NMR spectrum of 3F-PA·HI salt (**4**) SI-25

6. References SI-26

Experimental Section

2.1. Chemistry

The starting materials, reagents, and solvents employed were commercially available and were purchased from either Aldrich (Taipei, Taiwan) or SynQuest (FL, USA) and used as received. The purity of all the intermediates and products, were monitored by using gas chromatography/mass by utilizing an Agilent 6890 series gas chromatograph and series 5973 mass selective detector. Ligand synthesis was monitored with an HP 6890 GC using a 30−m HP−1 capillary column with a 0.25−μm stationary phase film thickness. The flow rate was 1 mL/min, and splitless injection was used. The TLC was done by using Merck Kieselgel 60 F254 aluminum plates. Infrared spectra were obtained using a Perkin Elmer RX I FT−IR spectrophotometer. NMR spectra were recorded on Bruker AM 600 and 300 spectrometers using 5−mm o.d sample tubes. $CDCl_3$, and DMSO−d_6 were the references for both ^{1}H and ^{13}C NMR spectra, while refrigerant−11 ($CFCl_3$) was the reference for ^{19}F NMR spectra. The coupling constants *J* are given in hertz (Hz).

2.2. Synthesis of tert-butyl (3-hydroxypropyl)carbamate (N-BOC-PA-OH) (1)

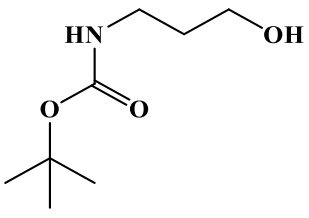

(1)

In a 1 L single-necked round-bottomed flask, 3-amino-1-propanol (5.0 g, 66 mmol) was dissolved in a mixture of CH_2Cl_2 (75 mL) and saturated aqueous Na_2CO_3 solution (14.1 g, 133 mmol) in H_2O (35 mL). Di-tert-butyl dicarbonate (15.99 g, 73 mmol) was then added to the mixture at 0 °C. The flask was loosely capped with a rubber septum that contained two needles to release CO_2 produced during the reaction. The mixture was stirred vigorously for 12h at room temperature under an ambient atmosphere. Afterward, the reaction mixture was poured over EtOAc. The organic phase was dried over anhydrous Na_2SO_4, filtered and concentrated under reduced pressure to yield a crude colorless oil (10.7 g, ~91.74%) of compound (**1**).

Analytical data of (**1**): Yield: 92%; ^{1}H NMR (300 MHz, $CDCl_3$, room temperature): δ (ppm)= 4.7 (1H, br, N<u>H</u>), 3.6 (2H, q, $^3J_{HH}$ = 5.4 Hz, PA-C<u>H</u>$_2$OH, Hc), 3.4 (2H, q, $^3J_{HH}$ = 6.0 Hz Ha), 3.0 (1H, br, O<u>H</u>), 1.6 (2H, quint, $^3J_{HH}$ = 6.0 Hz Hb), 1.4 (9H, s, *t*-butyl, Hd); FT-IR υ(cm^{-1}): 3348 ($\upsilon_{PA\text{-}CH2\underline{OH}}$), 3348 ($\upsilon_{PA\text{-}N\text{-}H}$), 2978, 2936, 2877, ($\upsilon_{PA\text{-}CH2}$), 1684 ($\upsilon_{C=O}$); GC/MS (m/z): 12.3 min, 175 (M^+), 118 (M^+ - *t*-butyl), 102 (M^+ - *t*-butoxide), 87 (M^+ - *t*-butyl – CH_2OH), 74 (M^+ - BOC), 57 (*t*-butyl$^+$).

2.3. Synthesis of tert-butyl (3-bromopropyl)carbamate (N-BOC-PA-Br) (2)

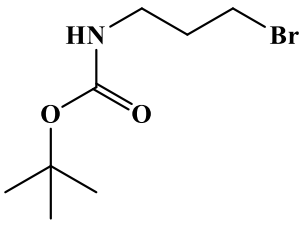

(2)

In a 250 mL single-necked round-bottomed flask containing a solution of compound (**1**) (5.0 g, 7.21 mmol), CBr_4 (14.49 g, 42.8 mmol) in THF (70 mL) was added Ph_3P (9.71 g, 37.1 mmol) in THF (60 mL) at 0 °C, and the mixture was stirred for 1h at 0°C. Additional CBr_4 (4.83 g, 14.3 mmol) and Ph_3P (4.12 g, 15.7 mmol) were added to the solution. Under an N_2 atmosphere, the resulting solution was stirred for 4h at room temperature until the starting material completely disappered on TLC. The resultant mixture was extracted three times with EtOAc and deionized H_2O. The combined organic layers were further purified with brine and deionized H_2O, dried over Na_2SO_4, filtered, and concentrated under reduced pressure to give the compound (**2**) (5.40 g, 79.5%) as a pale-yellow liquid.

Analytical data of (**2**): Yield: 90%; ^{1}H NMR (300 MHz, $CDCl_3$, room temperature): δ (ppm)= 4.6 (1H, br, N<u>H</u>), 3.4 (2H, t, $^{3}J_{HH}$ = 6.3 Hz, PA-C<u>H</u>$_2$Br, Hc), 3.2 (2H, q, $^{3}J_{HH}$ = 6.3 Hz Ha), 2.0 (2H, quint, $^{3}J_{HH}$ = 6.9 Hz Hb), 1.4 (9H, s, *t*-butyl, Hd); FT-IR υ(cm^{-1}): 3348 ($\upsilon_{PA\text{-}N\text{-}H}$), 2977, 2932, 2872, ($\upsilon_{PA\text{-}CH2}$), 1690 ($\upsilon_{C=O}$); GC/MS (m/z): 13.6 min, 239 (M^+), 180 (M^+ - *t*-butyl), 136 (M^+ - BOC), 101 (BOC), 57 (*t*-butyl $^+$).

2.4. Synthesis of *tert*-butyl (3-(2,2,2-trifluoroethoxy)propyl)carbamate (N-BOC-3F-PA) ligand (3)

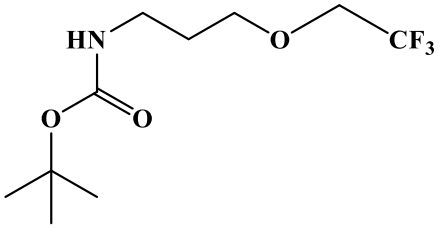

(3)

A 250 mL double-necked round-bottom flask was equipped a magnetic stirrer and a vacuum system. Air and moisture were removed from the flask using the vacuum system. To ensure the reaction system was under a nitrogen atmosphere, this process was repeated multiple times. CF_3CH_2OH (2.02 g, 20.2 mmol) and CH_3ONa (3.40 g, 18.9 mmol) were added to the flask. Under a N_2 atmosphere, this mixture was stirred overnight. The following day, the methanol was removed under vacuum, driving the reaction to the product side and leaving a white powder. Freshly distilled anhydrous THF (50 mL) was then added to the reaction flask under ice cooling in an external ice bath. Compound (**2**) **(**3.0 g, 12.6 mmol) was added to the reaction mixture, and the mixture was stirred for 24h while gradually warming to room temperature.[1-7] After confirming the formation of the ligand using GC/MS analysis, the reaction was quenched by adding water. The entire flask contents were transferred to a 1 L separatory funnel and extracted three times with CH_2Cl_2 and deionized H_2O. The organic phase was dried over Na_2SO_4 and concentrated under reduced pressure to yield compound (**3)** as a colorless liquid (2.3g, 71.0%).

Analytical data of (**3**): Yield: 71%; ^{1}H NMR (300 MHz, $CDCl_3$, room temperature): δ (ppm)= 4.7 (1H, br, N<u>H</u>), 3.8 (2H, q, $^{3}J_{HF}$ = 9 Hz, OC<u>H</u>$_2$CF$_2$, Hd), 3.6 (2H, t, $^{3}J_{HH}$ = 6.3 Hz, PA-OC<u>H</u>$_2$, Hc), 3.2 (2H, q, $^{3}J_{HH}$ = 6.3 Hz Ha), 1.7 (2H, quint, $^{3}J_{HH}$ = 6.3 Hz Hb), 1.4 (9H, s, *t*-butyl, He); FT-IR (cm^{-1}): 3356 ($\upsilon_{PA\text{-}N\text{-}H}$), 2979, 2934, 2879, ($\upsilon_{PA\text{-}CH2}$), 1693 ($\upsilon_{C=O}$), 1159, 1138 ($\upsilon_{CF3}$); GC/MS (m/z):

11.9min, 257 (M^+), 200 (M^+ - *t*-butyl), 184 (M^+ - *t*-butoxide), 156 (M^+ - BOC), 117 (M^+ - *t*-butyl - CH_2CF_2H), 102 (M^+ - *t*-butyl - OCH_2CF_2H), 83 ($C_2H_2CF_3$), 73 (C_3H_7NO), 57 (*t*-butyl$^+$).

2.5. Synthesis of 3-(2,2,2-trifluoroethoxy)propaylammonium iodide salt (3F-PA·HI) (4)

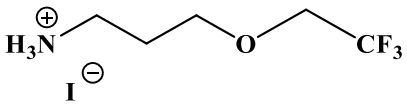

(4)

Compound (**3**) (1.0 g, 3.9 mmol) was added to a 100 mL round-bottomed flask, and CH_2Cl_2 (20 mL) was added to dissolve it. To the solution, 57 wt% hydroiodic acid (1.54 mL, 11.7 mmol) without a stabilizer was added in an ice bath. The reaction mixture was stirred under N_2 (g) at 40 °C for 2 hr. The solvent was then removed under vacuum, and the product was washed thoroughly with Et_2O.[8,9] Finally, the product was dried under vacuum for several days to yield a shiny white powder of compound (**4**) (also abbreviated as 3F-PA·HI).

Analytical data of (**4**): Yield: 60-70%; ^{1}H NMR (300 MHz, $CDCl_3$, room temperature): δ (ppm) = 7.8-7.4 (3H, PA-N$\underline{H}_3^+$), 3.9 (2H, q, $^3J_{HF}$ = 9 Hz, OC$\underline{H}_2CF_3$, Hd), 3.8 (2H, t, $^3J_{HH}$ = 5.7 Hz, PA-C$\underline{H}_2$O, Hc), 3.3 (2H, m, $^3J_{HH}$ = 6.3 Hz Ha), 2.1 (2H, quint, $^3J_{HH}$ = 6.3 Hz Hb); ^{13}C NMR (150 MHz, DMSO-d_6, room temperature): δ (ppm)= δ=125.9 - 124.1 (1C, m,-$\underline{C}F_3$), 69.1 (1C, s, PA-$\underline{C}$H2O-), 67.8 - 67.1 (1C, q, ^2JCF = 32.9 Hz, -O$\underline{C}H_2CF_3$), 36.8 (1C, s, $\underline{C}H_2$-NH$^+$), 27.6 (1C, s, -$CH_2\underline{C}H_2CH_2$); ^{19}F NMR (564 MHz, DMSO-d_6, room temperature): δ (ppm)= -72.8 (3F, s ,-C$\underline{F}_3$); FT-IR υ(cm^{-1}): 3202, 3024 ($\upsilon_{PA\text{-}N\text{-}H}$), 2975, 2932, 2887 ($\upsilon_{PA\text{-}CH2}$), 1580 ($\upsilon_{PA\text{-}N\text{-}H\text{-}bend}$), 1151, 1112 ($\upsilon_{CF3}$).

2.6. Preparation of (3F-PAH)$_2$PbI$_4$ 2D perovskite precursor solution

To prepare the (3F-PAH)$_2$PbI$_4$ precursor solution, a 2:1 stoichiometric ratio of PbI_2 (46.2 mg, 0.1 mmol) and 3F-PA·HI (57.1 mg, 0.2 mmol) were dissolved in an *N*,*N*-dimethylformamide (DMF) solvent at ambient condition. The obtained 2D perovskite precursor, the solution was stirred at 50 °C for 3 hr and then allowed to cool down to room temperature before use.

2.7. Characterization of (3F-PAH)$_2$PbI$_4$ perovskite. The crystallographic structure information of (3F-PAH)$_2$PbI$_4$ was characterized using a Rigaku XtaLAB Synergy DW single crystal diffractometer equipped with a HyPix-Arc 150° curved Hybrid Photon Counting X-ray detector and Micro Max-007 HF microfocus rotating anode with dual wavelength (Cu and Mo). The phases of HP film were measured using a PAN alytical Empyrean powder X-ray diffractometer with Cu-K_α source radiation and equipped with PIXcel^{1D} detector. The diffraction patterns were collected in the 2θ range of 5° to 80° with a step size of

0.01°. The high-resolution field emission scanning electron microscopic (FESEM) images were taken by Hitachi-SU8100 instrument. The atomic force microscopy (AFM) image was taken by FSM, Nano view 1000 instrument. The thickness of the $(3F\text{-}PAH)_2PbI_4$ film was measured using a VHX-6000 digital microscope. The absorption spectrum of the $(3F\text{-}PAH)_2PbI_4$ film was recorded by a JASCO V670 spectrophotometer. The photoluminescence (PL) spectrum (excitation at 400 nm) was measured with a JASCO FP-8500 spectrofluorometer. Time-resolved photoluminescence (TRPL) was obtained from an PicoQuant PicoHarp 300 instrument with Picoquant LDH series picosecond pulse laser diode (405 nm, 0.36 μW). Additionally, electrochemical data were obtained by cyclic voltammetry (CV) using a using an electrochemical work station CH instrument (CHI-6041E) consisting of three electrodes where glassy carbon was used as the working electrode, Ag/AgCl (NaCl) was the reference electrode, and platinum wire was used as the counter electrode.

2.8. Device fabrication and measurements

The SiO_2/Si substrate was cleaned in ethanol, acetone, and deionized water in series using an ultrasonic bath. For device fabrication, 5 nm/95 nm of Ti/Au was deposited on the paper through electron beam evaporation with interdigitated electrode patterns defined by a shadow mask. The width and interspace width of the interdigital electrode used for device preparation are 995 μm and 30.8 μm, respectively. Then the 100 μl of prepared $(3F\text{-}PAH)_2PbI_4$ perovskite precursor solution was deposited onto the surface of the SiO_2/Si substrate by one-step spin coating technique with a spin rate of 2000 rpm for 30 s. During the process, the film turned from pale yellow to orange in a few seconds as the solvent evaporated. After spin coating, the prepared film was quickly removed from the spin coater and the film has annealed on the top of a hot plate at 50 °C for 15 min. Finaly, the electrical and optoelectronic properties of the $(3F\text{-}PAH)_2PbI_4$ were characterized using a semiconductor analyzer (Keithley 2612) under dark and laser light illumination conditions in ambient conditions. Power tunable laser with wavelength of 450 nm was used to characterize the photo-responses and other optoelectronic properties of the devices. The light powers were measured by a power meter (LP10, SANWA, Japan).

2.9. Computational methods: The geometry of $3F\text{-}PAH^+$ is optimized by the density functional theory (DFT)[10] at the B3LYP/6-311G(d)[11,12] level. All calculations are performed in the Gaussian 16 package.[13] and output files are visualized by its GaussView 6.0.16 program.[14] Electrostatic potential (ESP) calculations were completed to validate the formation of σ-hole region. The highest occupied molecular orbitals (HOMO), the lowest unoccupied molecular orbitals (LUMO) and molecular dipole moment were also computed for the $3F\text{-}PAH^+$ cationic spacer.

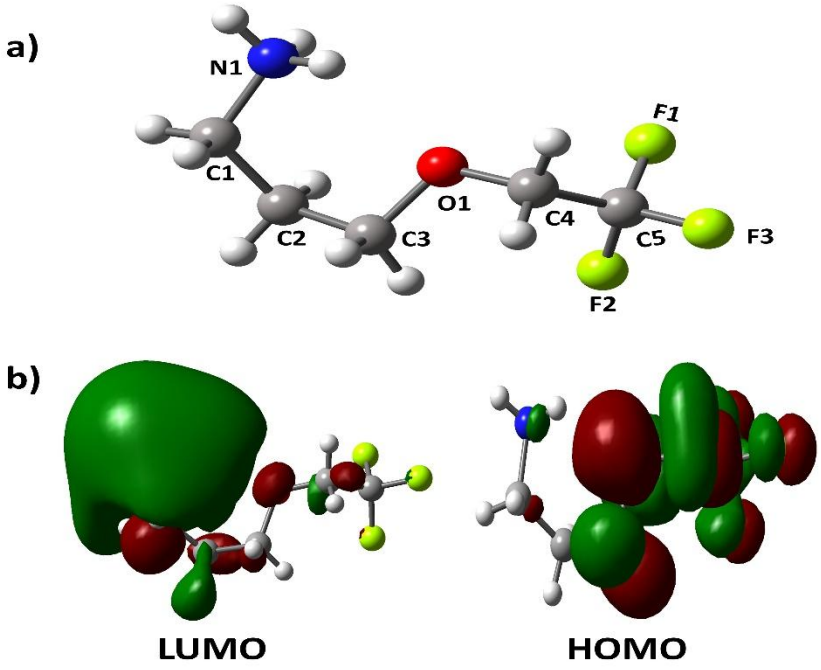

Figure S1. a) The optimized structure of the fluorinated aliphatic linearly-chained 3F-PAH$^+$ organic cation, b) highest occupied molecular orbital (HOMO) and lowest unoccupied molecular orbital (LUMO) diagrams of 3F-PAH$^+$ spacer.

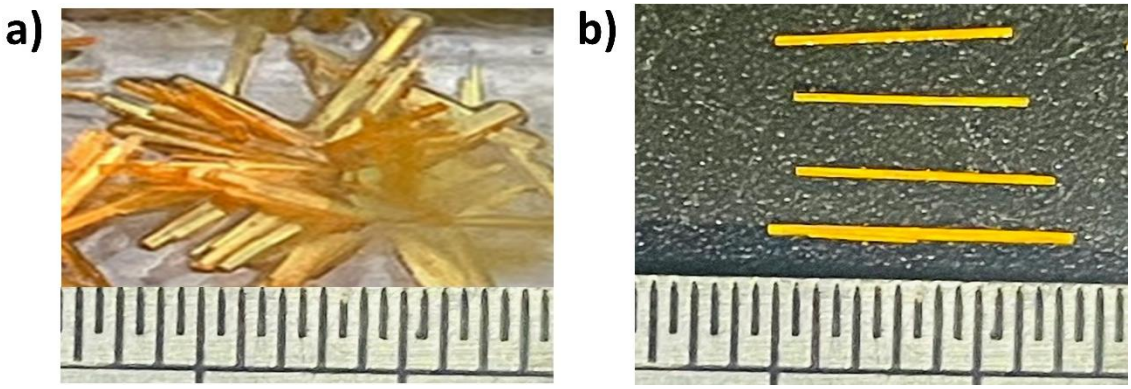

Figure S2. The photographs of the synthesized fluorinated $(3F\text{-}PAH)_2PbI_4$ HP single-crystals. a) the bundles of crystals and b) 4 pieces of its single crystals oriented horizontally.

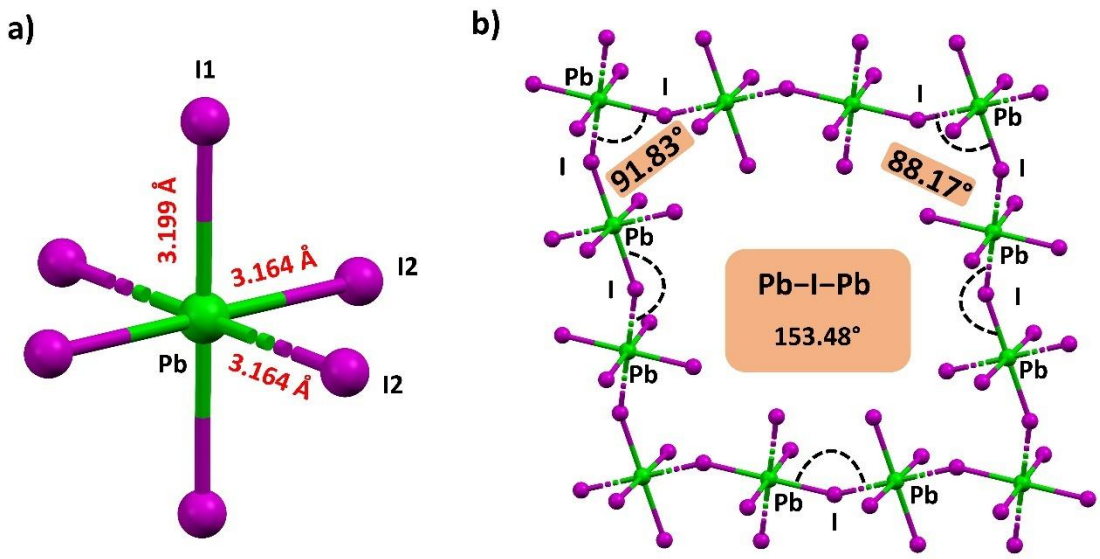

Figure S3. The single-crystal structure of $(3F\text{-}PAH)_2PbI_4$ showing a) the core unit of $[PbI_6]^{4-}$ octahedra with Pb−I bond lengths and b) the I−Pb−I bond.

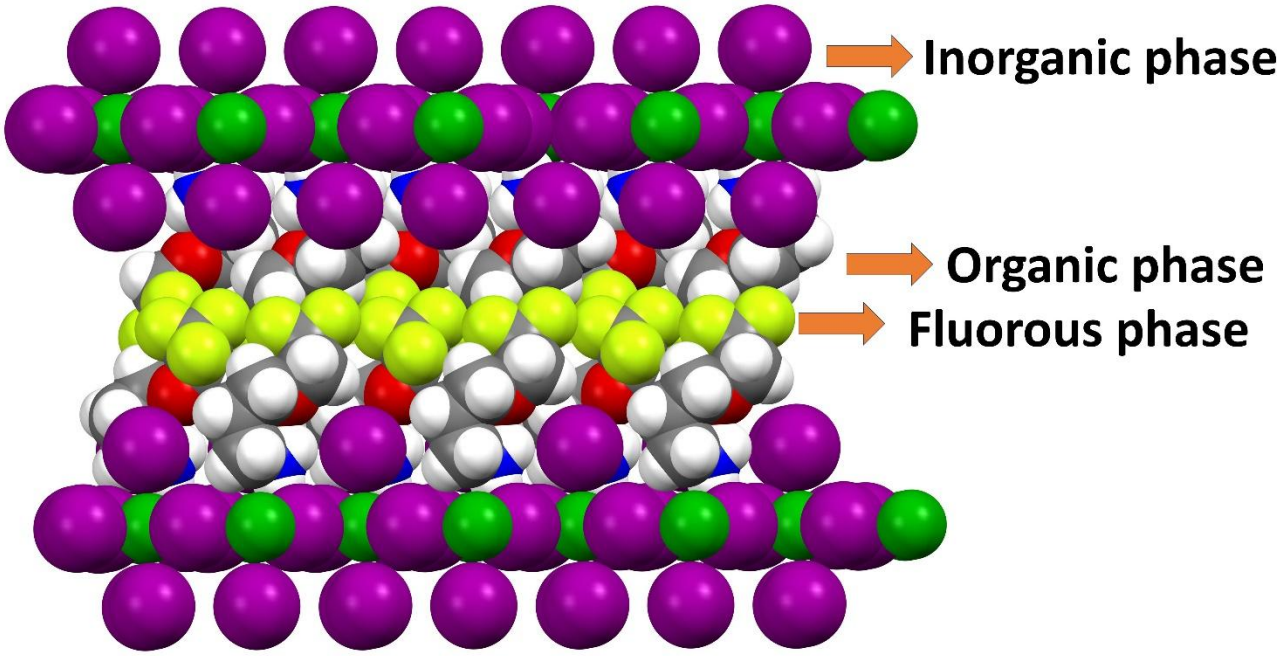

Figure S4. The packing mode with the space-filling view of $(3F\text{-}PAH)_2PbI_4$ HP showing an inorganic phase of $[PbI_6]^{4-}$ octahedra and both the organic and fluorous phase from the $3F\text{-}PAH^+$ organic cations.

$$D = \frac{K\lambda}{\beta cos\theta} \quad \text{(S1)}$$

where K is the Scherrer constant, λ is the x-ray wavelength (1.5406 Å), β is the full width at half maximum (FWHM) in radians, and θ is the half of the Bragg angle.

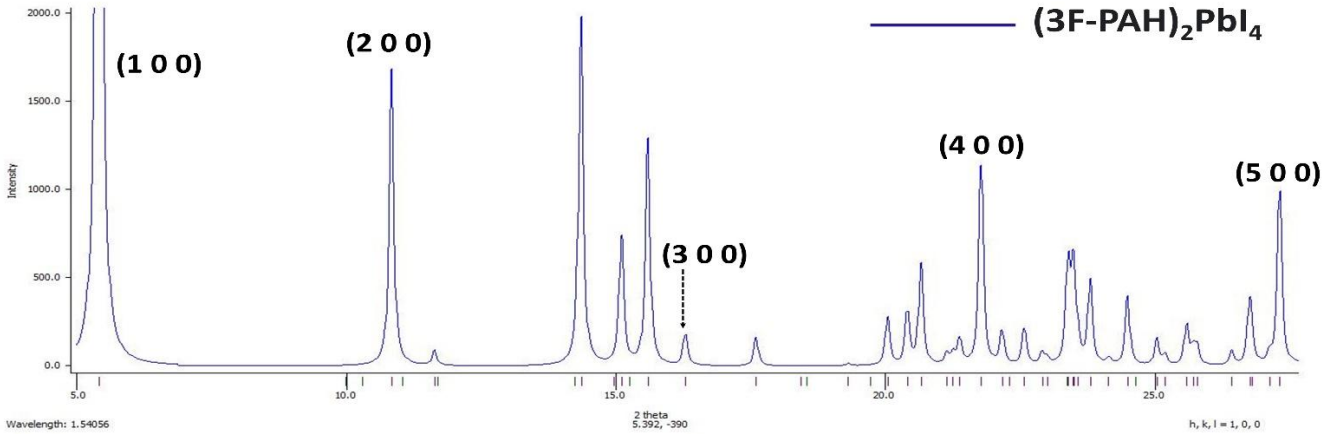

Figure S5. The simulated PXRD pattern of fluorinated $(3F\text{-}PAH)_2PbI_4$ HP from its 3D x-ray CIF.

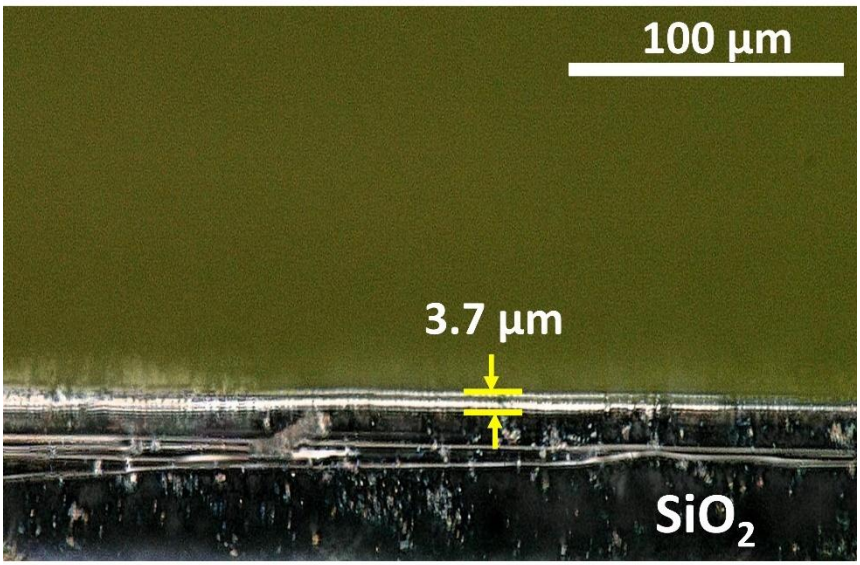

Figure S6. The optical microscope image showing the thickness of the $(3F\text{-}PAH)_2PbI_4$ HP film.

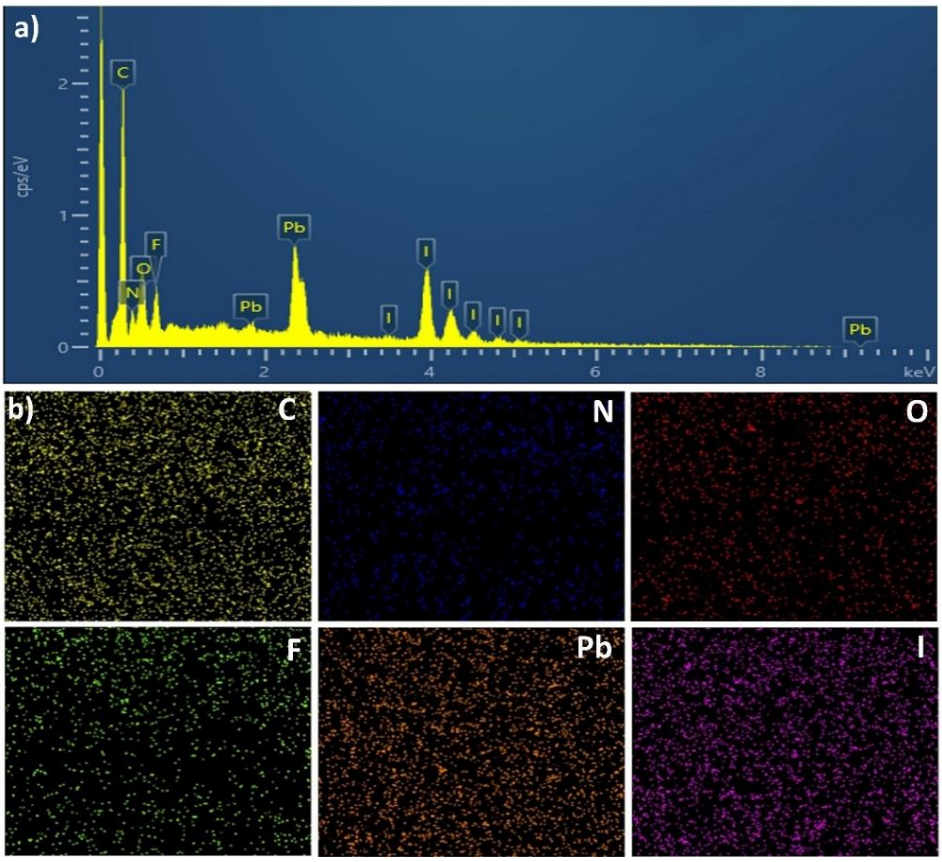

Figure S7. a) EDS spectrum and b) EDS-mapping of the fluorinated $(3F\text{-}PAH)_2PbI_4$ HP film showing a uniform distribution of all elements (C, N, O, F, Pb and I).

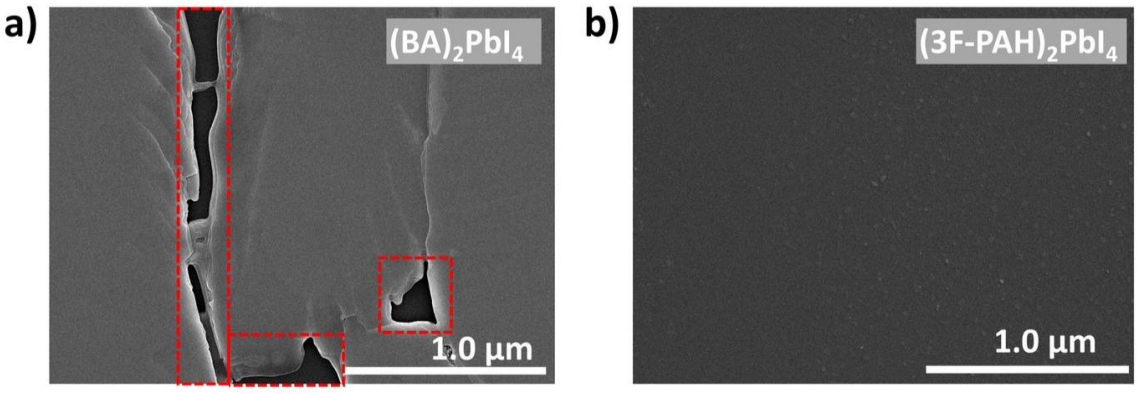

Figure S8. The surface morphologies of the 2D HPs showing a) top-view SEM image of aliphatic $(BA)_2PbI_4$ HP film and b) top view SEM image of fluorinated $(3F\text{-}PAH)_2PbI_4$ HP film.

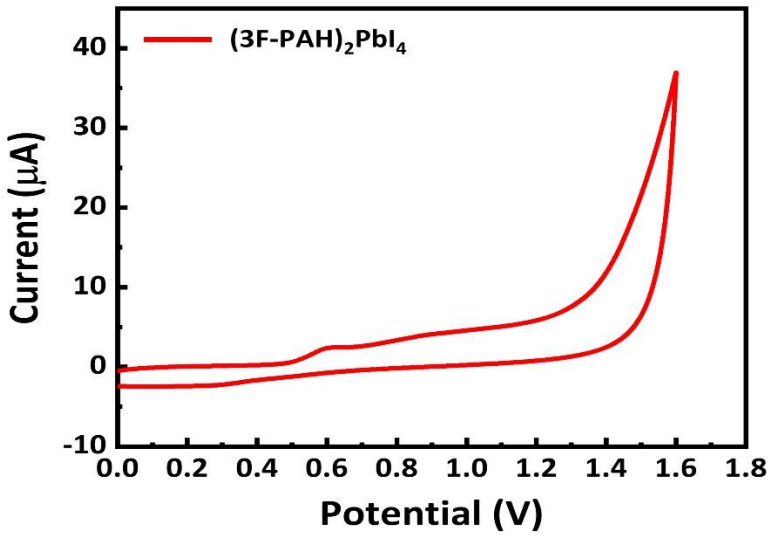

Figure S9. Cyclic voltammetry (CV) profile of fluorinated $(3F\text{-}PAH)_2PbI_4$ HP, showing an oxidation potential (E_{ox}) of 0.59 eV which is be readily observed from the ground state.

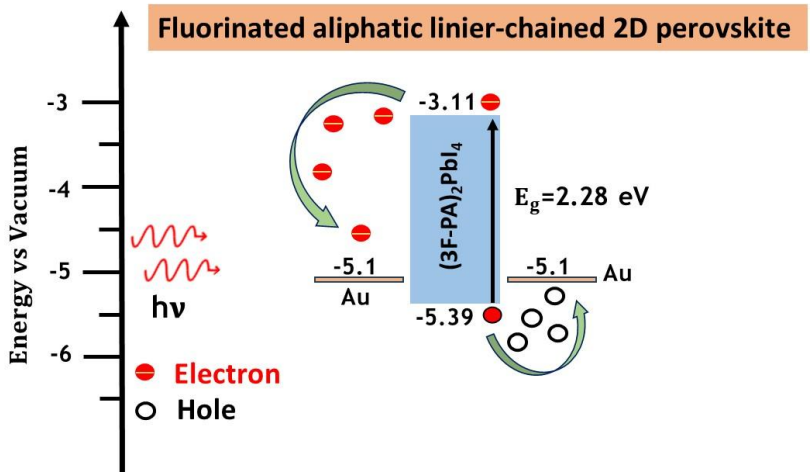

Figure S10. Schematic energy band diagram of the $(3F\text{-}PAH)_2PbI_4$ HP.

The highest occupied molecular orbitals (HOMO) and the lowest unoccupied molecular orbitals (LUMO) of this fluorinated $(3F\text{-}PAH)_2PbI_4$ HP were calculated by the CV curve and E_g with the equations[9] shown below:

$$E_{HOMO} = -[E_{ox} + 4.80] \quad \text{(S2)}$$

$$E_{LUMO} = E_{HOMO} + E_g \quad \text{(S3)}$$

where E_{ox}, which is the obvious oxidation potential from the ground state, is used to calculate HOMO [= -(4.80+0.59) eV] using Eq. S2; and for LUMO calculation: energy bandgap, E_g, is obtained from the Tauc plot (i.e. E_g= 2.28 eV). Then LUMO= -5.39 + 2.28= -3.11 (eV).

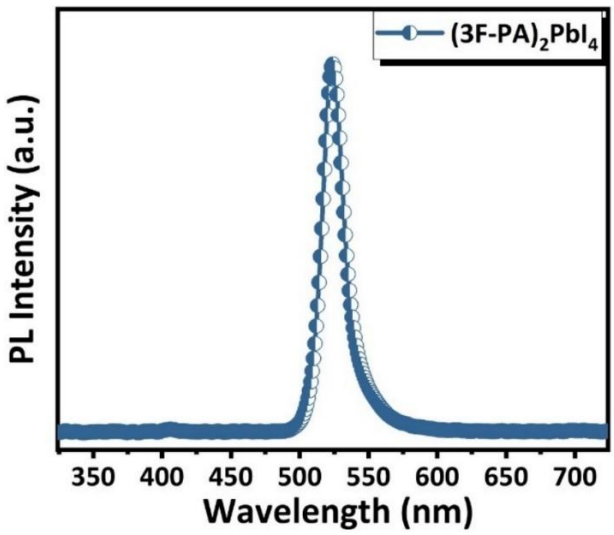

Figure S11. The photoluminescence (PL) spectrum of the fluorinated $(3F\text{-}PAH)_2PbI_4$ HP film.

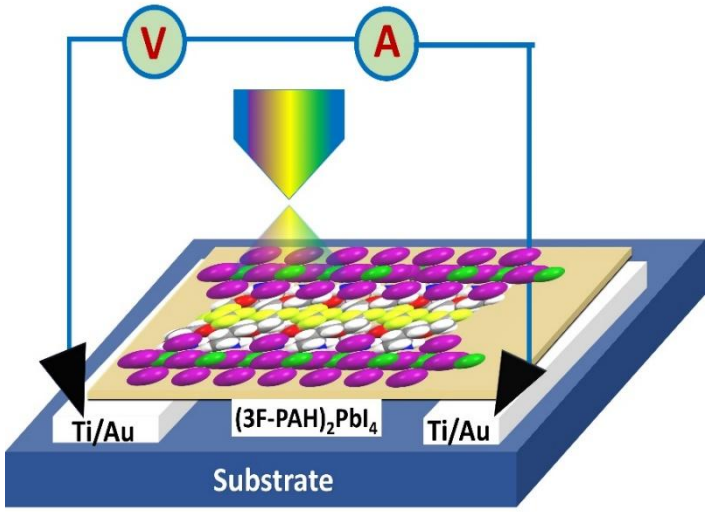

Figure S12. Schematic drawing of the fabricated $(3F\text{-}PAH)_2PbI_4$ HP photodetector device.

The responsivity (R) of $(3F\text{-}PAH)_2PbI_4$ HP photodetector device is calculated based on equation S4.[9]

$$\boldsymbol{R} = \frac{\boldsymbol{I_{ph} - I_{dark}}}{\boldsymbol{A \times P_{in}}} \quad \text{(S4)}$$

Where I_{ph} and I_{dark} represents the photocurrent and dark current, respectively. The A is the effective area ($=1.770 \times 10^{-4}$ cm^2) of the PD. The P_{in} is the incident laser power per unit area of the PD.

The detectivity (D^*) of $(3F\text{-}PAH)_2PbI_4$ HP photodetector device is calculated based on equation S5[9]

$$D^* = R\sqrt{\frac{A}{2qI_{dark}}} \quad \text{(S5)}$$

Where q is the unit electron charge, A is the effective area (=1.770 × 10^{-4} cm^2) of the device and I_{dark} is the dark current.

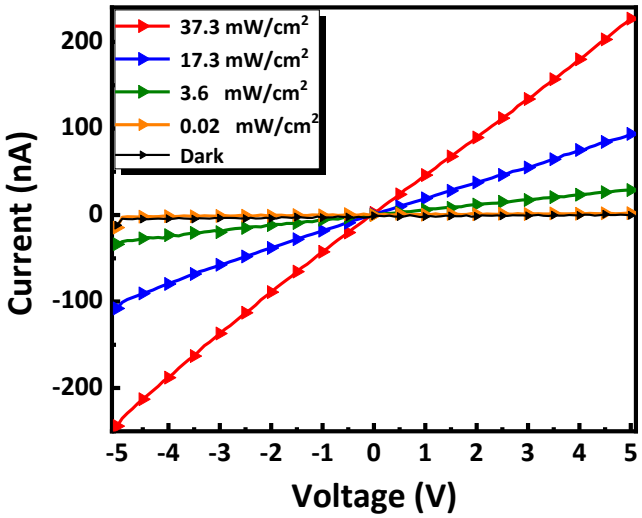

Figure S13. *I-V* characteristics of the fluorinated $(3F\text{-}PAH)_2PbI_4$ HP photodetector device under dark conditions and upon 450 nm illumination at different power densities.

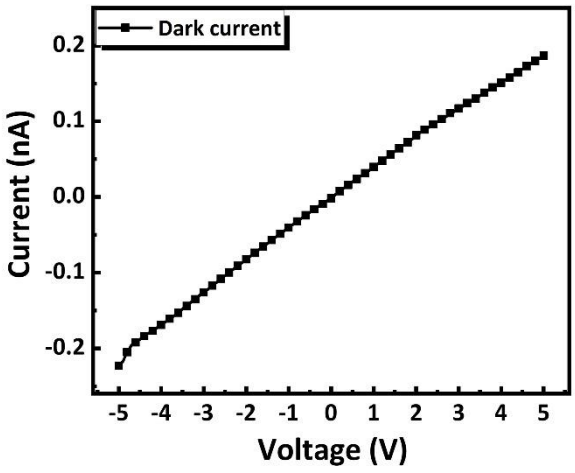

Figure S14. *I-V* characteristics of the fluorinated $(3F\text{-}PAH)_2PbI_4$ HP photodetector device under dark conditions.

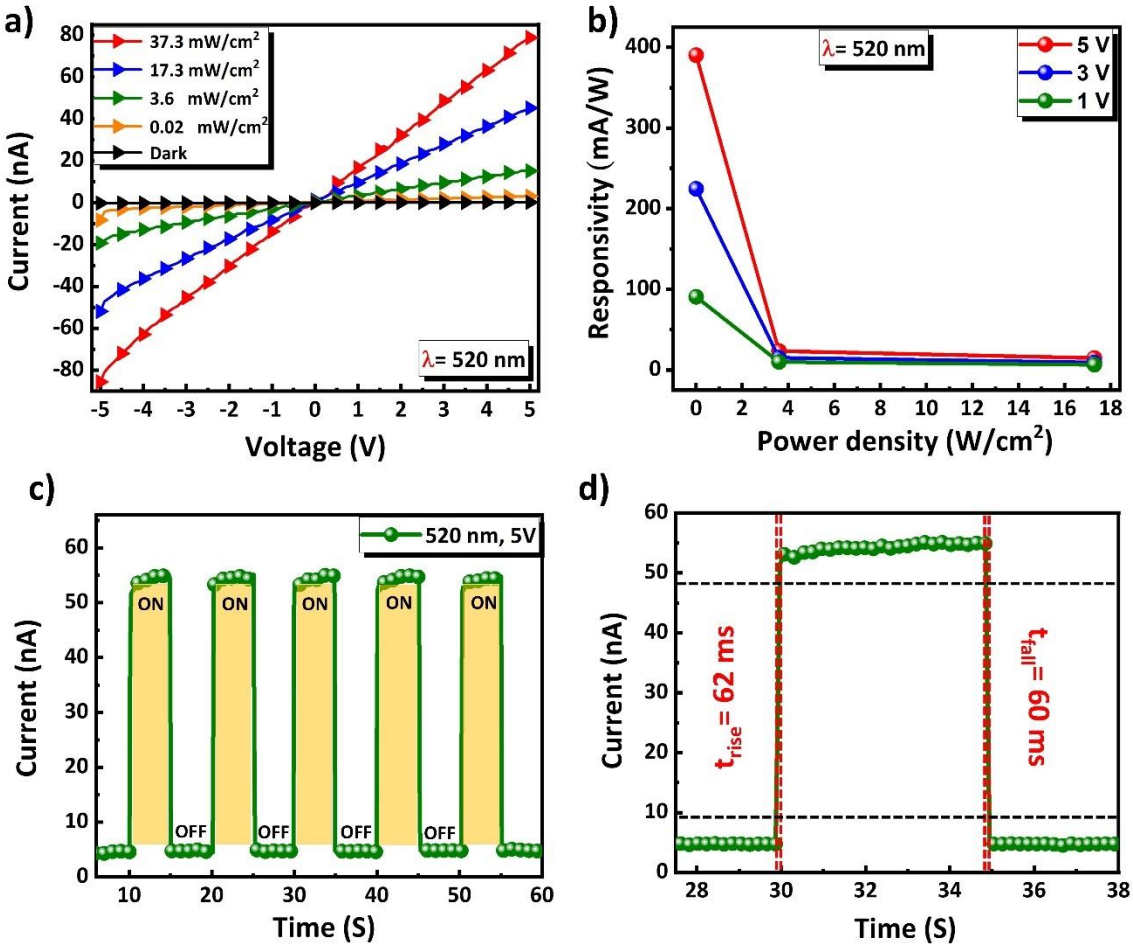

Figure S15. The photodetection performance of fluorinated $(3F\text{-}PA)_2PbI_4$ HP PD device under 520 nm showing a) *I-V* characteristics under dark state and with different powers, b) responsivity at different illumination powers at different applied bias, c) time-dependent photocurrent response, and d) *I–t* curve in a cycle.

1. Structural table section

Table S1: X-ray crystallographic data and structure refinement for $(3F\text{-}PAH)_2PbI_4$ HP

Crystal data	
CCDC	2415016
Chemical formula	$PbI_4 \cdot 2(C_5H_{11}F_3NO)$
μ_r	1031.08
Crystal system, space group	Monoclinic, $P2_1/c$
Temperature (K)	100
a, b, c (Å)	16.3481(3),8.5891(1),8.8735(1)
β (°)	93.927 (1)
V (Å^3)	1243.05 (3)
Z	2
Radiation type	Cu $K\alpha$
μ (mm^{-1})	52.69
Crystal size (mm)	0.29 × 0.18 × 0.09
Data collection	
Diffractometer	Bruker *APEX*-II CCD
Absorption correction	Multi-scan [a]
T_{min}, T_{max}	0.001, 0.02
No. of measured, independent and observed [$I > 2s(I)$] reflections	6974, 2392, 2154
R_{int}	0.042
$(\sin \theta/\lambda)_{max}$ (Å^{-1})	0.621
Refinement	
$R[F^2 > 2s(F^2)]$, $wR(F^2)$, S	0.033, 0.087, 1.04
No. of reflections	2392
No. of parameters	117
No. of restraints	0
H-atom treatment	H-atom parameters constrained
$D\rho_{max}$, $D\rho_{min}$ (e Å^{-3})	3.51, -1.68

a) CrysAlis PRO 1.171.42.51a (Rigaku Oxford Diffraction, 2022).

Table S2. Selected bond lengths of fluorinated $(3F\text{-}PAH)_2PbI_4$ HP (at 100 K).

Bond	**Bond length (Å)**	**Bond**	**Bond length (Å)**
Pb1—I2^{i}	3.168(0)	F2—C5	1.335(8)
Pb1—I2^{ii}	3.176(0)	F3—C5	1.340(8)
Pb1—I2	3.168(0)	C1—H1D	0.990
Pb1—I2^{iii}	3.176(0)	C1—H1E	0.990
Pb1—I1^{i}	3.199(0)	C1—C2	1.522(9)
Pb1—I1	3.199(0)	C2—H2A	0.990
N1—H1A	0.910	C2—H2B	0.990
N1—H1B	0.910	C2—C3	1.490(10)
N1—H1C	0.910	C3—H3A	0.990
N1—C1	1.493(8)	C3—H3B	0.990
O1—C4	1.411(8)	C4—H4A	0.990
O1—C3	1.447(8)	C4—H4B	0.990
F1—C5	1.336(8)	C4—C5	1.501(9)

Symmetry codes: (i) -*x*, -*y*+1, -*z*+1; (ii) -*x*, *y*-1/2, -*z*+3/2; (iii) *x*, -*y*+3/2, *z*-1/2; (iv) -*x*, *y*+1/2, -*z*+3/2.

Table S3. Selected bond angles of fluorinated $(3F\text{-}PAH)_2PbI_4$ HP (at 100 K).

Bond	**Bond angle (°)**
$I2^{i}$—Pb1—I2	180.00
I2—Pb1—$I2^{ii}$	88.17(0)
$I2^{i}$—Pb1—$I2^{ii}$	91.83(0)
$I2^{i}$—Pb1—$I2^{iii}$	88.17(0)
I2—Pb1—$I2^{iii}$	91.83(0)
$I2^{iii}$—Pb1—$I2^{ii}$	180.00
$I2^{ii}$—Pb1—I1	90.51(1)
$I2^{i}$—Pb1—I1	87.13(1)
$I2^{ii}$—Pb1—$I1^{i}$	89.49(1)
I2—Pb1—$I1^{i}$	87.13(1)
$I2^{iii}$—Pb1—I1	89.49(1)
$I2^{iii}$—Pb1—$I1^{i}$	90.50(1)
$I2^{i}$—Pb1—$I1^{i}$	92.87(1)
I2—Pb1—I1	92.87(1)
$I1^{i}$—Pb1—I1	180.00
Pb1—I2—$Pb1^{iv}$	153.48(1)

Symmetry codes: (i) -*x*, -*y*+1, -*z*+1; (ii) -*x*, *y*-1/2, -*z*+3/2; (iii) *x*, -*y*+3/2, *z*-1/2; (iv) -*x*, *y*+1/2, -*z*+3/2.

Table S4. N−H···I and C−H···X type of hydrogen bonds in fluorinated $(3F\text{-}PAH)_2PbI_4$ HP (at 100 K).

Item	**Hydrogen bond**	**D–H (Å)**	**H···A (Å)**	**D···A (Å)**	**<DHA (°)**
1	N1−H1A···I1^{i}	0.91	2.75	3.64	168
2	N1−H1B···I1^{ii}	0.91	2.92	3.70	121
3	N1−H1C···I2	0.91	2.92	3.66	139
4	N1−H1B···O1	0.91	2.23	2.81	121
5	C3−H3B···F2	0.99	2.54	3.13	118

Symmetry codes: (i) x,-1+y,z, 1/2+z; (ii) x,3/2-y,1/2+z.

Table S5. Comparison of selected structural (Pb−I−Pb angle) and optical properties (bandgap**)** of fluorinated linearly-chained $(3F\text{-}PAH)_2PbI_4$ RP HP with other fluorinated 2D RP HPs.

No.	Materials	UV-Vis Bandgap (eV)	Pb−I−Pb Angle (°)	Ref.
1	$(PEA)_2PbI_4$	2.37	151.44 152.90	15
2	(*p*F PEA)$_2$PbI$_4$	2.37	151.41	
3	(*o*F-PEA)$_2$PbI$_4$	2.36	150.50	16
		2.62	148.70	
4	(*m*F-PEA)$_2$PbI$_4$	2.35	151.00	
5	(*p*F-PEA)$_2$PbI$_4$	2.32	152.98	
6	$(CF_3\text{-}PMA)_2PbI_4$	2.52	145.89	17
7	$(5FBzA)_2PbI_4$	2.52	149.73 150.46	18
8	$(EA)_2PbBr_4$	2.93	150.53	19
9	$(2FEA)_2PbBr_4$	3.04	144.03	
10	$(L_f)_2PbI_4$	2.60	144.73	20
11	**$(3F\text{-}PAH)_2PbI_4$**	**2.28**	**153.48**	**This work**

Note: PEA- phenylethylammonium, *x*PEA- phenylethylammonium (*x* = *ortho*, *meta* and *para*), *x*PMA-phenylmethylammonium (*x* = CF_3), 5FBzA-pentafluorobenzyl ammonium, EA-ethylammonium, 2FEA-2,2-difluoroethylammonium and L_f- $C_9H_6F_{13}NH_3^+$.

Table S6. The crystallite size of fluorinated $(3F\text{-}PAH)_2PbI_4$ HP calculated using the Scherrer equation.

Peak	θ (degree)		FWHM (radian)		D (nm)	
	PXRD	Simulated data from CIF	PXRD	Simulated data from CIF	[i]D1 (PXRD)	[ii]D2 (Simulated data)
1	2.7657	2.7076	0.0014	0.0018	99.1540	77.1141
2	5.4487	5.4241	0.0014	0.0017	99.4880	81.9259
3	8.1366	8.1477	0.0014	0.0018	100.0456	77.8134
4	10.8485	10.9040	0.0016	0.0016	88.2356	88.2498
5	13.5855	13.6626	0.0018	0.0016	79.2473	89.1800
Average crystallite size					**93.2341**	**82.8265**

Note i: The average crystallite size, D1, is calculated from the PXRD pattern (see Figure 1d in the main content). Note ii: D2 is determined from the simulated PXRD pattern from CIF (see Figure S5 above) based on the single-crystal structure of $(3F\text{-}PAH)_2PbI_4$ HP

Table S7. Comparison of hydrophobic and hydrophilic interactions and their effects on the performance, morphology, and stability of perovskite materials in optoelectronic applications.

Aspect	Hydrophobic interactions[26]	Hydrophilic interactions
Definition[a]	These improper HB interactions occur when a hydrogen attached to a less electronegative atom. (e.g., C, Si, P, B etc.). Take C for example, then the sp^3 C-H bond is known to be non-polar.	These HB interactions occur when a hydrogen attached to an electronegative atom. (-i.e., F, O and N.) Take O for example, then the resulting O-H bond is known to be a very polar.
Type[b]	C–H···X type, where X is usually an element with good electronegativity and can provide the lone electron pair. Because C-H bond is non-polar, the typical hyperconjugation step then does not take place. It is rehybridization that dominates instead. Thus, the sp^3 C-H bond is not dissociated. e.g. C–H···X [C–H···F, C–H···O, C–H···N, and C–H···I(-M).	X–H···Y type, where X is the strongly electronegative; Y is usually the element with high electronegativity and can provide the lone electron pair. e.g. N–H···O, O–H···O and O–H···N.
Morphology	Providing compact, uniform, pinhole-free hydrophobic films with reduced grain boundaries.	Usually leading to the increased grain boundaries and potential voids due to water absorption, affecting film uniformity.
Stability	Enhancing moisture resistance by creating the hydrophobicity and water-repellent fluorous layer, thus greatly improving moisture stability.	Increasing susceptibility to moisture-induced degradation due to water absorption, compromising stability.
Impact on optoelectronic performance	Improving charge transport by reducing trap states and non-radiative recombination; the induced large dipole moment enhances device performance.	Leading to the increased trap states and charge recombination due to moisture absorption, reducing device performance.

Note: [a]Because the hydrogen bonding interactions (HBs) are the main weak non-covalent interactions in this fluorinated HP material, the comparisons of hydrophobic and hydrophilic interactions in this table are mainly based on HBs. [b] In addition to the C–H···X type of non-classical hydrophobic hydrogen-bonding (HB) interactions, the C–F···F and C–F···O halogen-bonding (XB) interactions can also contribute to enhance the hydrophobicity of the materials.

Table S8. Comparison of fitting parameters for time-resolved photoluminescence (TRPL) for the fluorinated $(3F\text{-}PAH)_2PbI_4$ HP film with other structurally similar 2D HPs structures reported previously.

Item	Sample	τ_1 (ns)	A_1 (counts)	τ_2 (ns)	A_2 (counts)	$\tau_{(ave)}$ (ns)	Ref.
1	$(BA)_2PbI_4$	0.40	1673.37	2.78	19.65	0.81	21
2	$(HA)_2PbI_4$	0.50	1394.42	4.14	55.75	1.40	
3	$(OA)_2PbI_4$	0.55	1201.92	6.47	24.57	1.70	
4[a]	$(BA)_2PbI_4$	301.00	3429.60	57.30	6496.50	236.90	25
5[a]	$(FBA)_2PbI_4$	166.80	2793.40	23.30	5155.20	137.30	
6	**$(3F\text{-}PAH)_2PbI_4$**	**0.18**	**8350.00**	**1.20**	**475.00**	**0.46**	**This work**

Note: [a]The items 4 & 5 were used in the preparation of 2D/3D perovskites, which are applied in solar cell fabrication.

To investigates the fast charge transfer and charge carrier dynamics in a newly fabricated fluorinated linearly-chained $(3F\text{-}PAH)_2PbI_4$ HP film, we have conducted time-resolved photoluminescence (TRPL) under a 405 nm laser to study the carrier dynamic information shown in Figure 3e and Table S8. We fit the TRPL curves using a biexponential reconvolution model (see equation S6 and S7 in SI). As shown in Figure 3e, the average carrier lifetime (τ_{ave} = 0.46 ns), which is significantly shorter than those of BA_2PbI_4 (0.81 ns), HA_2PbI_4 (1.40 ns), and OA_2PbI_4 (1.70 ns). Additionally, as shown in items 4 &5 (in Table S8), the τ_{ave} of BA_2PbI_4 is 236.90 ns, while the τ_{ave} fluorinated BA_2PbI_4 (FBA_2PbI_4) shows the faster lifetime of 137.30 ns.[21] These results can be used affirm that the incorporation of the polyfluorinated chain into the organic spacer can significantly eliminate the non-radiative recombination ratio induced by the trap centers, resulting in a fast charge transfer. Thus, these results reveal that the CF_3-containing organic spacer can effectively reduce the non-radiative recombination ratio caused by the trap centers which then help to make the charge transfer fast. The detailed comparisons of trifluoromethyl group-incorporated aliphatic linearly-chained $(3F\text{-}PAH)_2PbI_4$ HP with other structurally similar HPs (BA, FBA, HA, and OA) from literature are described in Table S8.

We fit the TRPL curves using a triexponential re-convolution model shown below:

$$I(t) = \int_{-\infty}^{t} IRF\,(t') \sum_{i=1}^{n} A_i \exp\left(-\frac{t-t'}{\tau_i}\right) dt' \qquad \text{(S6)}$$

where $\tau_{1,}$ and τ_2 are the slow and fast decay time, respectively; and A_1 and A_2 are their corresponding decay amplitudes. The average decay time has been calculated using the following equation (in S7):

$$\sigma_\tau = \frac{\sum_{i=1}^{n} A_i \tau_i^2}{\sum_{i=1}^{n} A_i \tau_i} \qquad \text{(S7)}$$

2. The NMR spectra (H-, F-, C-NMR) of prepared compounds (1-4).

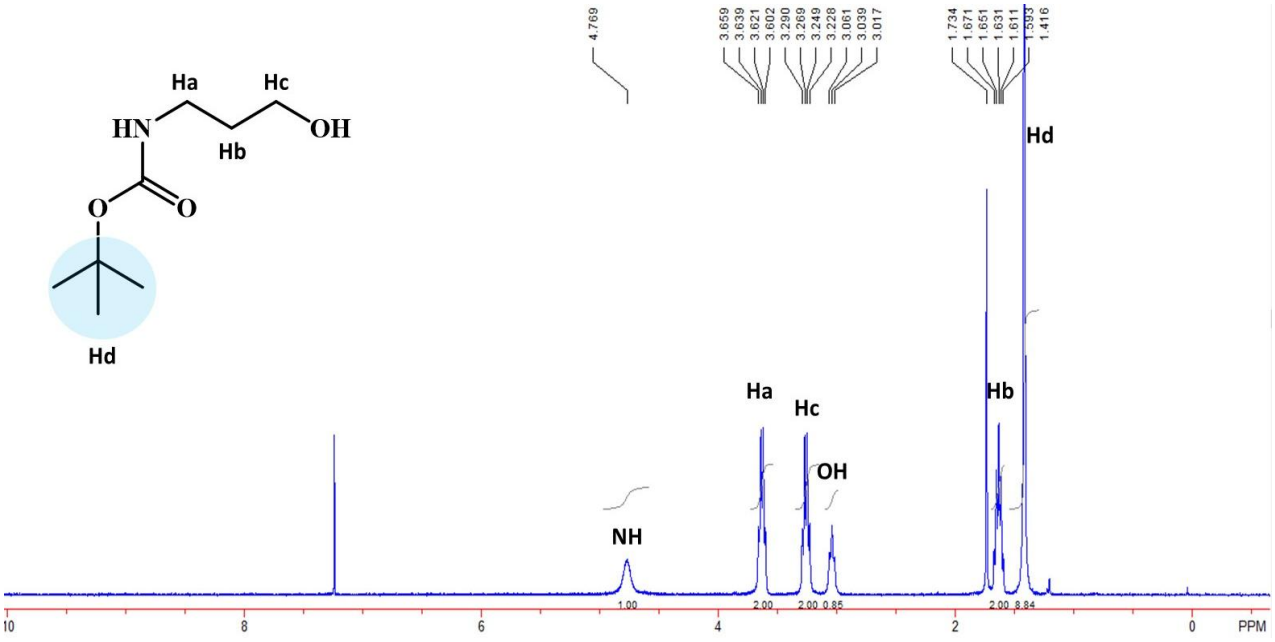

Figure S16. ^{1}H NMR spectrum of the N-BOC-PA-OH (in $CDCl_3$).

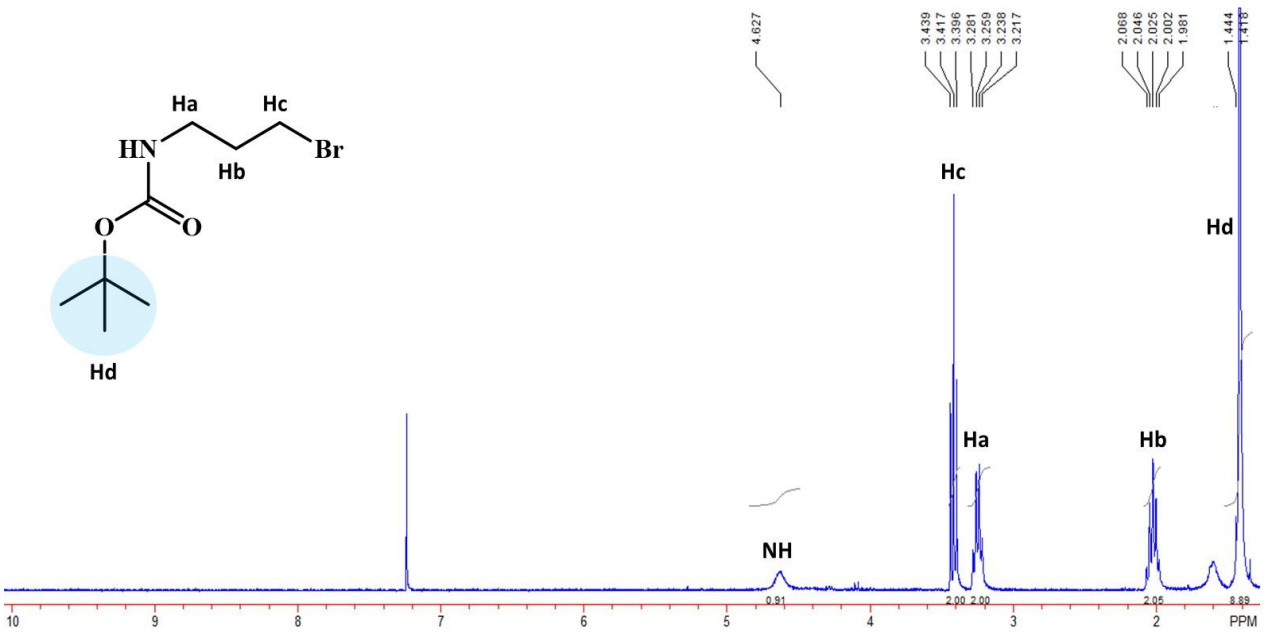

Figure S17. ^{1}H NMR spectrum of the N-BOC-PA-Br (in $CDCl_3$).

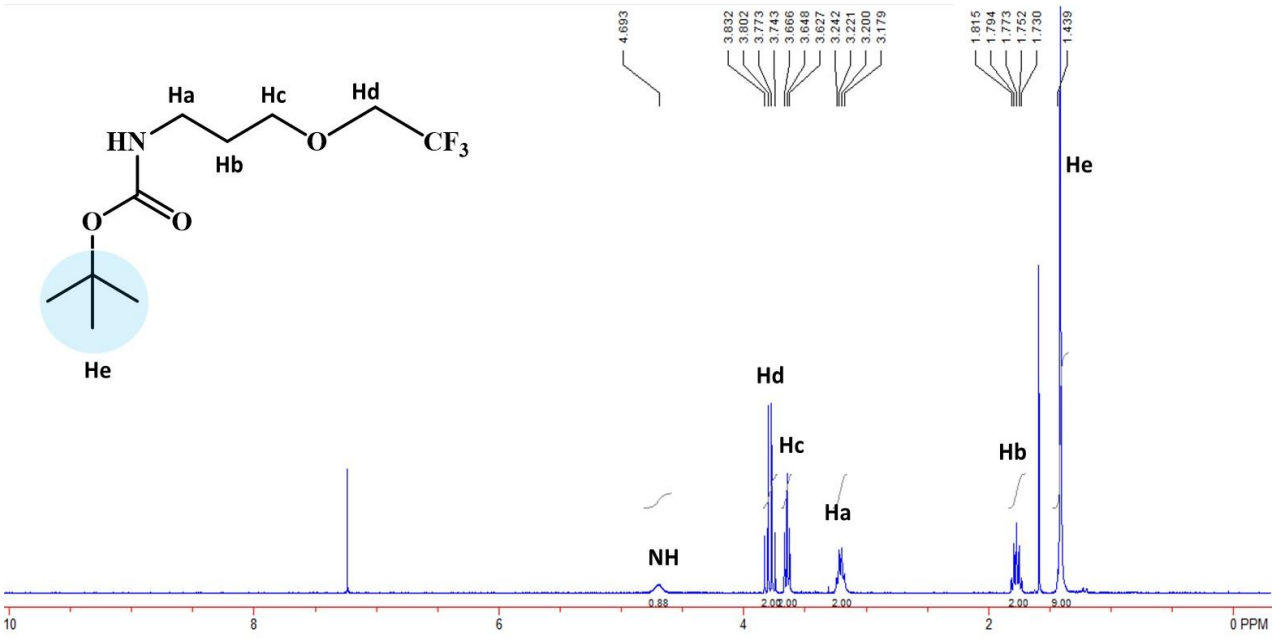

Figure S18. ^{1}H NMR spectrum of the N-BOC-3F-PA-ligand (in $CDCl_3$).

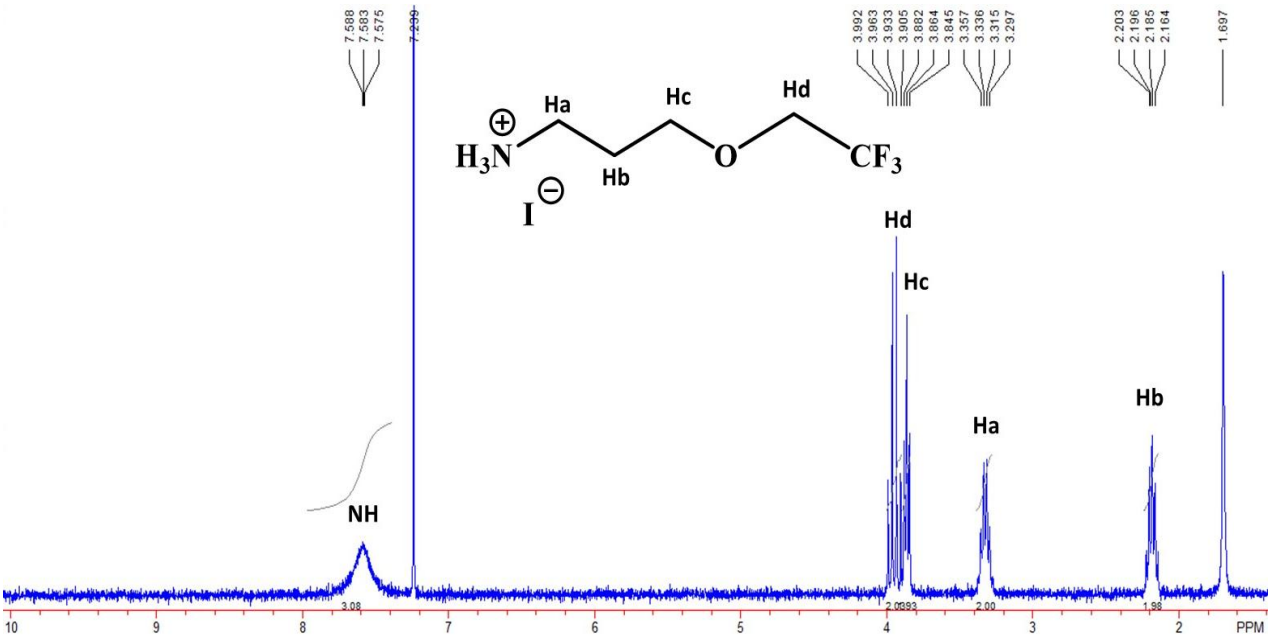

Figure S19. ^{1}H NMR spectrum of the 3F-PA·HI salt (in $CDCl_3$).

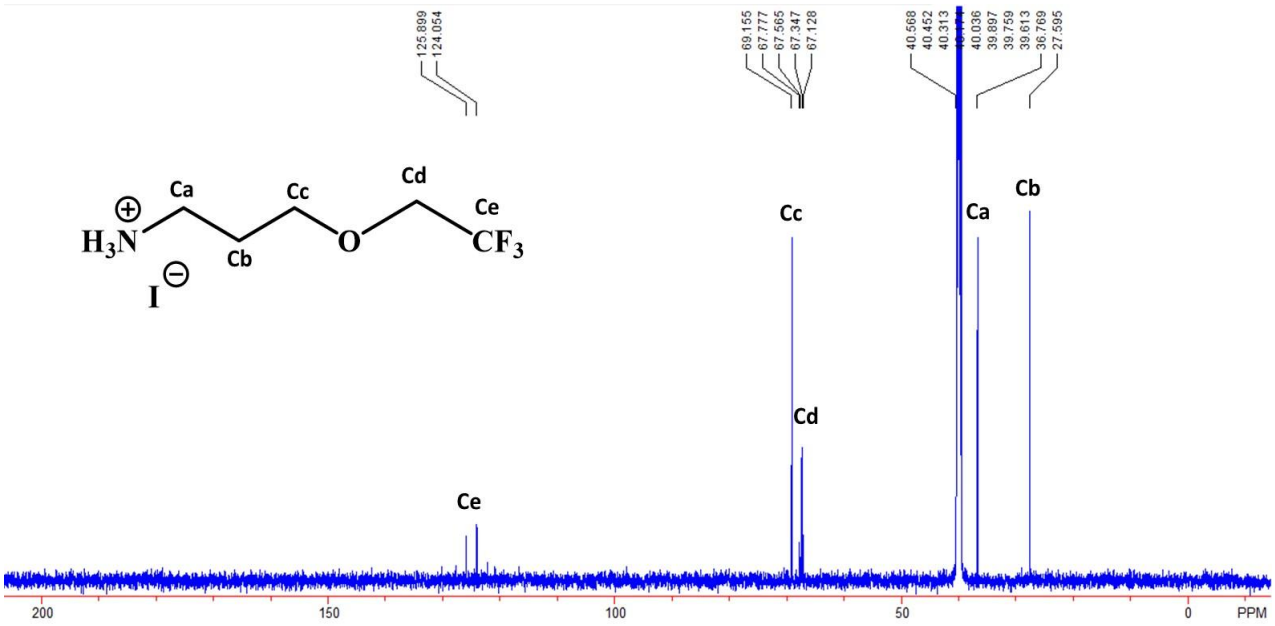

Figure S20. ^{13}C NMR spectrum of the 3F-PA·HI salt (in DMSO-d_6).

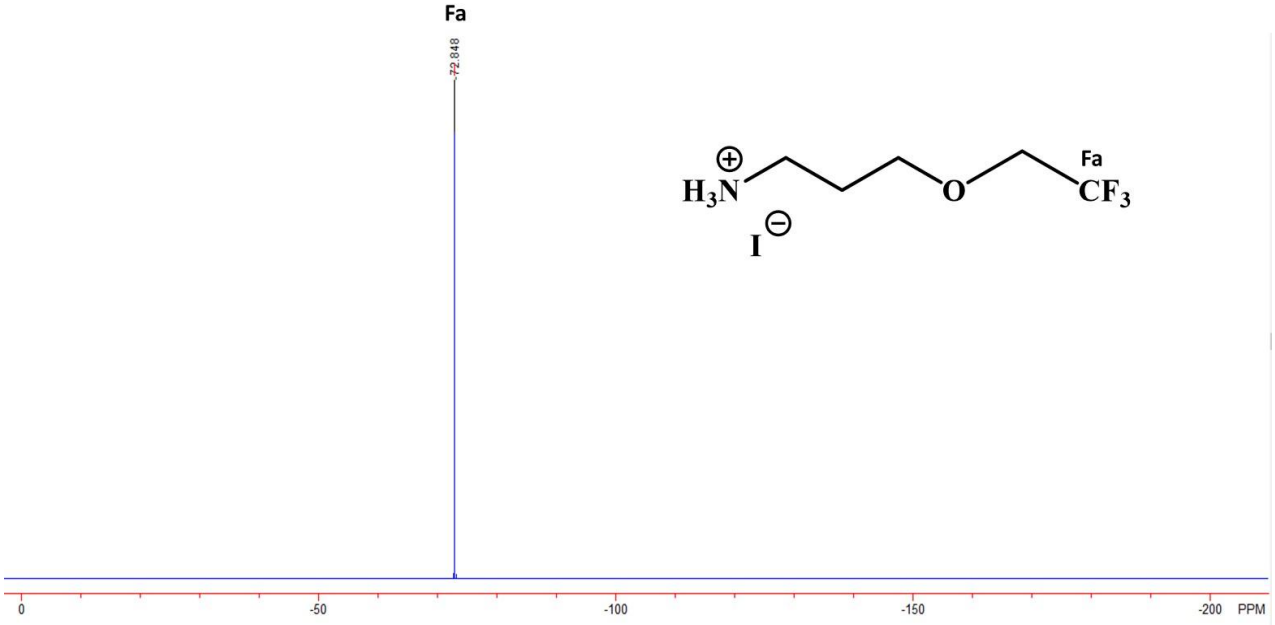

Figure S21. ^{19}F NMR spectrum of the 3F-PA·HI salt (in DMSO-d_6).

References

(1) N. Lu, Y.-C. Lin, J.-Y. Chen, C.-W. Fan, L.-K. Liu, *Tetrahedron,* 2007, **63**, 2019.

(2) J. L. Howell, N. Lu, C. M. Friesen, *J. Fluor. Chem.*, 2005, **126**, 281.

(3) N. Lu, J. Chen, C. Fan, Y. Lin, Y. Wen, L. Liu, *J. Chinese Chem. Soc.,* 2006, **53**, 1517.

(4) N. Lu, Y.-M. Ou, T.-Y. Feng, W.-J. Cheng, W.-H. Tu, H.-C. Su, X. Wang, L. Liu, M. D. Hennek, T. S. Sayler, J. S. Thrasher, *J. Fluor. Chem.,* 2012, **137**, 54.

(5) N. Lu, K.-Y. Lin, C.-K. Li, C.-C. Kung, Y.-P. Yeh, Y.-Y. Cheng, L.-K. Liu, *J. Chinese Chem. Soc.*, 2015, **62**, 64.

(6) N. Lu, W.-H. Tu, H.-C. Hou, C.-T. Lin, C.-K. Li, L.-K. Liu, *Polyhedron* 2010, **29**, 1123.

(7) V. Elakkat, C.-C. Chang, J.-Y. Chen, Y.-C. Fang, C.-R. Shen, L.-K. Liu, N. Lu, *Chem. Commun.*, 2019, **55**, 14259.

(8) L. Mao, W. Ke, L. Pedesseau, Y. Wu, C. Katan, J. Even, M. R. Wasielewski, C. C. Stoumpos, M. G.Kanatzidis, *J. Am. Chem. Soc.*, 2018, **140**, 3775.

(9) N. Lu, G. Gurumallappa, J. Singh, K.L. Chan, E. Tessema, P.Y. Liu, M.K. Hema, C.S. Karthik, J.H. Ho, Y.C. Chao, L.G.H. Dao, *ACS Appl. Mater. Interfaces*, 2025, **17**, 1743.

(10) E. Runge, E. K. U. Gross, *Phys. Rev. Lett.*, 1984, **52**, 997.

(11) A.D. Becke, *J. Chem. Phys.*, 1992, **96**, 2155.

(12) P. C. Hariharan, J. Pople, A. *Mol. Phys.*, 1974, **27**, 209.

(13) M.E. Frisch, G.W. Trucks, H.B. Schlegel, G.E. Scuseria, M.A. Robb, J.R Cheeseman,. G. Scalmani, V.P.G.A. Barone, G.A. Petersson, H.J.R.A. Nakatsuji, X. Li, 2016, Gaussian 16, revision C. 01.

(14) R. Dennington, T. Keith, J. Millam, 2009, GaussView, version 5.

(15) D. B. Straus, N.Iotov, M. R. Gau, Q. Zhao, P. J. Carroll, C. R. Kagan, *J. Phys. Chem. Lett.*, 2019, **10**, 1198.

(16) J. Song, X. Feng, H. Wei, B. Yang, *Adv. Funct. Mater.,* 2022, **32**, 2203329.

(17) P.-X Wang, A.M. Najarian, Z. Hao, A. Johnston, O. Voznyy, S. Hoogland, E. H. *J* Sargent, *Phys. Chem. Lett.*, 2020, **11**, 10144.

(18) S. Paek, C. Roldán-Carmona, K.T. Cho, M. Franckevičius, H. Kim, H. Kanda, N. Drigo, K. Lin, M. Pei, R. Gegevičius, H. J. Yun, H. Yang, P.A. Schouwink, C. Corminboeuf, A.M. Asiri, M.K. Nazeeruddin, *Adv. Sci.*, 2020, **7**, 2001014.

(19) Luo, B.; Guo, Y.; Xiao, Y.; Lian, X.; Tan, T.; Liang, D.; Li, X.; Huang, X. *J. Phys. Chem. Lett.*, 2019, **10**, 5271.

(20) I. García-Benito, C. V. I. E. Quarti, Queloz, Y.J. Hofstetter, D. Becker-Koch, P. Caprioglio, D. Neher, S. Orlandi, M. Cavazzini, G. Pozzi, J. Even, M.K. Nazeeruddin, Y. Vaynzof, G. Grancini, *Front. Chem.*, 2020, **7**, 946.

(21) G. Liu, C. Qiu, B. Tian, X. Pan, D. Ding, Y. Chen, C. Ren, T. He, Y. Shi, C. Su, Y. Li, Y. Gao, D. Fan, *ACS Appl. Mater. Interfaces*, 2019, **1**, 2253.

(22) J. Zhou, Y. Chu, J. Huang, *ACS Appl. Mater. Interfaces*, 2016, **8**, 25660.

(23) R. dong, C. Lan, X. Xu, X. Liang, X. Hu, D. Li, Z. Zhou, L. Shu, S. Yip, C. Li, S.-W.Tsang, J. C. Ho, *ACS Appl. Mater. Interfaces*, 2018, **10**, 19019.

(24) G. R. Perumallapelli, T. Tsuda, P. Formanek, N. Kiriy, V. Bakulev, F. Simon, B. Voit, S. C. B. Mannsfeld, A. Kiriy, *Org. Electron.*, 2020, **87**, 105935.
(25) T. Niu, J. Lu, X. Jia, Z. Xu, M.C. Tang, D. Barrit, N. Yuan, J. Ding, X. Zhang, Y. Fan, T. Luo, *Nano lett.*, 2019, **19**, 7181.
(26) N. Lu, V. Elakkat, J. S. Thrasher, X. Wang, E. Tessema, K. L. Chan, R.-J. Wei, T. Trabelsi and J. S. Francisco, *J Am Chem Soc*, 2021, **143**, 5550–5557.